

Flow structure and evaporation behavior of an acoustically levitated droplet

K. Kobayashi, A. Goda, K. Hasegawa, and Y. Abe

Citation: *Physics of Fluids* **30**, 082105 (2018); doi: 10.1063/1.5037728

View online: <https://doi.org/10.1063/1.5037728>

View Table of Contents: <http://aip.scitation.org/toc/phf/30/8>

Published by the [American Institute of Physics](#)

Articles you may be interested in

[Hydrodynamics experiments with soap films and soap bubbles: A short review of recent experiments](#)

Physics of Fluids **29**, 111113 (2017); 10.1063/1.4986003

[Aerodynamic characteristics of unsteady gap flow in a bristled wing](#)

Physics of Fluids **30**, 071901 (2018); 10.1063/1.5030693

[Supercritical fluid flow dynamics and mixing in gas-centered liquid-swirl coaxial injectors](#)

Physics of Fluids **30**, 075106 (2018); 10.1063/1.5026786

[Vibrational modes prediction for water-air bubbles trapped in circular microcavities](#)

Physics of Fluids **30**, 082001 (2018); 10.1063/1.5037328

[Drainage, rebound and oscillation of a meniscus in a tube](#)

Physics of Fluids **30**, 082103 (2018); 10.1063/1.5038662

PHYSICS TODAY

WHITEPAPERS

ADVANCED LIGHT CURE ADHESIVES

Take a closer look at what these environmentally friendly adhesive systems can do

READ NOW

PRESENTED BY
 MASTERBOND
ADHESIVES | SEALANTS | COATINGS

Flow structure and evaporation behavior of an acoustically levitated droplet

K. Kobayashi,^{1,a)} A. Goda,¹ K. Hasegawa,² and Y. Abe³

¹Graduate School of System and Information Engineering, University of Tsukuba, 1-1-1 Tennoudai, Tsukuba, Ibaraki, Japan

²Department of Mechanical Engineering, Kogakuin University, 2665-1 Nakanomachi, Hachioji, Tokyo, Japan

³Faculty of Engineering, Information and Systems, University of Tsukuba, 1-1-1 Tennodai, Tsukuba, Ibaraki, Japan

(Received 26 April 2018; accepted 19 July 2018; published online 6 August 2018)

We experimentally investigate the flow structure and evaporation behavior of a droplet in an ~ 19 kHz single-axis acoustic levitator. Decane, nonane, octane, heptane, hexane, and pentane are used as test fluids to investigate the effect of saturated vapor pressure on the internal and external flow fields. Under low saturated vapor pressure (decane and nonane), the direction of the external flow is away from the surface of the droplet. However, at a relatively higher saturated vapor pressure (octane, heptane, hexane, and pentane), the direction of the external flow is toward the surface of the droplet, with vortices forming near the droplet surface. For droplets with a low saturated vapor pressure (decane, nonane, octane, and heptane), the internal flow is similar to that in the case of rigid body rotation. Finally, under high saturated vapor pressure (hexane and pentane), the internal flow is an unsteady 3D complex flow. The experimental results indicate that the vapor concentration distribution around a levitated droplet surface correlates closely with changes in the external and internal flows. *Published by AIP Publishing.* <https://doi.org/10.1063/1.5037728>

I. INTRODUCTION

Using the acoustic levitation method (ALM), it is possible to trap,^{1,2} transport,³ and coalesce samples.⁴ Recently, enhanced capabilities within ALM have opened up new possibilities in acoustic manipulations in analytical chemistry,⁵ biology,⁶ and other areas.⁷ The advantage of acoustic levitation is that there are no strict requirements on the electrical and magnetic properties of the levitated sample.⁸ To date, there have been several studies on the hydrodynamic behavior of acoustically levitated droplets.^{9–16}

Puskar *et al.*¹⁷ reported that the Raman acoustic levitation spectroscopic approach can be used to monitor heme dynamics within a levitated 5-ml suspension of red blood cells and also to detect hemozoin in malaria-infected cells. Xie *et al.*¹⁸ showed that a living animal can be acoustically levitated. Sundvik *et al.*¹⁹ suggested that acoustic levitation for less than 2000 s does not interfere with the development of zebrafish embryos, but may affect their mortality rate. Their results showed that acoustic levitation could potentially be used as a non-contacting wall-less platform for characterizing and manipulating vertebrate embryos without causing major adverse effects on their development. Chainani *et al.*²⁰ developed a pulsed electrostatic delivery system that enables the addition and mixing of a droplet of desired volume with an acoustically levitated droplet. Bouyer *et al.*²¹ introduced bio-acoustic levitation technology for the direct assembly of multilayer 3D geometries within one single hydrogel construct.

Perfect sample manipulation using acoustic levitation has recently been highly anticipated, but it has not yet been realized, partly due to nonlinearities such as large deformations,^{22,23} multi-scale acoustic streaming,^{24–28} heat transfer,²⁹ and mass transport.^{30,31} Determining the nonlinear mechanisms and elucidating the phenomena in acoustically levitated droplets are crucial for perfect sample manipulation. Although there are many studies related to the transport phenomena of the levitated droplet,^{32–41} physical correlation between the hydrodynamic behavior across the boundary layer of the droplet interface and the phase change behavior from the droplet interface is still a remaining issue.⁴² To develop container-less processing techniques using the ALM, the interaction between the hydrodynamic behavior and the phase change behavior across the acoustically levitated droplet surface must be investigated.

We previously conducted experiments to understand the interaction between acoustic streaming and evaporation of a levitated droplet.^{43,44} We clarified that both internal and external flows depend on the saturated vapor pressure of a levitated droplet. Therefore, it is vital to obtain the volatile sample concentration near the external surface of a levitated droplet. In the present study, interferometry techniques were used to clarify the interaction between the gas flow generated by sound waves and the evaporation from an acoustically levitated droplet. Interferometry techniques have a wide range of applications in many industries. However, these techniques have not often been applied to thermo-fluid dynamics due to environmental restrictions. To obtain the concentration of a volatile sample surrounding a levitated droplet, a Mach–Zehnder interferometer was used. The method proposed by Kreis was used to identify the density (or concentration) difference around a

^{a)}Author to whom correspondence should be addressed: s1720933@s.tukuba.ac.jp

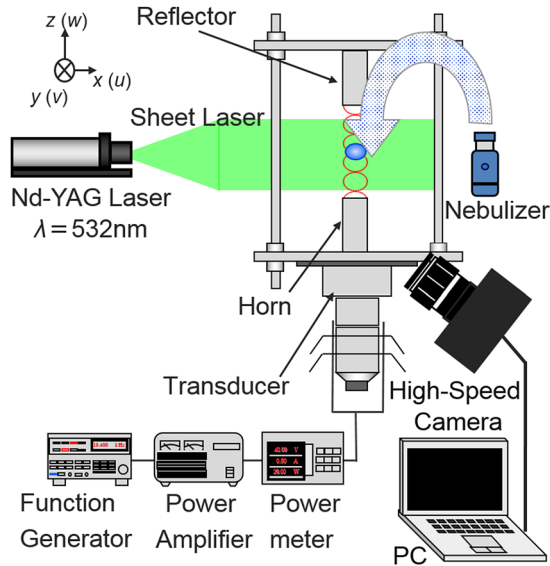


FIG. 1. Schematic of the acoustic levitation apparatus.

levitated sample.⁴⁵ The interference fringes were imaged using a high-speed camera. Each fringe image was analyzed using the Fourier transform method to extract the phase difference between the object and reference beams for each individual pixel, which corresponds to the refractive index in the droplet zone at that point. This process gives the 2D distribution of the refractive index in the droplet zone. The phase difference contains information on changes in the vapor concentration as a result of evaporation from the droplet. The velocity and vortex thickness in the vicinity of the droplet surface were also measured using particle image velocimetry (PIV) and particle tracking velocimetry (PTV). These properties were then compared with the refractive index distribution related to the vapor concentration distribution as determined using the Mach–Zehnder interferometer.

II. METHODS AND MATERIALS

A. Experimental setup and test fluids

Figure 1 shows a schematic diagram of the acoustic levitation apparatus used in this study. The experimental apparatus constituted a droplet levitation apparatus and measurement devices. A sinusoidal signal was generated using a function generator and inputted into an ultrasonic transducer through a power meter and an amplifier. The wave frequency was ~ 19 kHz. The ultrasonic wave was transmitted from the horn,

which was connected to the transducer, which on reflection formed a standing wave. The distance between the horn and the reflector was ~ 47 mm. Droplets were injected using a syringe and were levitated at a pressure node of the standing wave.

Herein, the external and internal flows associated with a levitated droplet were measured using visualization. To visualize the external flow, $5\text{-}\mu\text{m}$ -diameter tracer particles were generated using a nebulizer (OMRON Co., NE-U 22). To visualize the internal flow, $10\text{-}\mu\text{m}$ -diameter nylon tracer particles were contained within the droplets. The flow patterns were recorded using a high-speed video camera (Photron Co., FASTCAM-mini UX 100). PIV was implemented, and the quantitative flow field was imaged using a sheet laser (Japan Laser Co., DPGL-5W-L).

Six types of fluids were used for individual levitated droplets, to investigate how evaporation affected the internal and external flows. Table I lists the physical properties of the samples at 300 K. The saturated vapor pressures of the six fluids range from 207 to 73 168 Pa. The experiments were performed under ambient temperature and pressure.

To predict the concentration field around the volatile sample, a Mach–Zehnder interferometer was constructed (Fig. 2). The refractive index of the transparent fluid near the external surface of each levitated droplet was measured. The refractive index corresponds to the concentration of the fluids around the levitated droplet. The laser was of He–Ne type with a wavelength of 632.8 nm and an output power of 1 mW. The optical path incorporated a spatial filter, collimator, half mirror, mirror, neutral density filter (Kenko Tokina Co., 52S PRO-ND2, 4, 8), and a high-speed camera. The laser beam diameter was 25 mm. The object beam was adjusted to pass through a node of the standing wave. The reference beam passed through the air, and the object beam passed through the droplet in the test section. Interference fringes formed at the image plane of the camera, and images were then captured using the high-speed camera.

B. Velocity and vortex thickness measurement methods

We applied PTV to measure the flow velocity in the vicinity of the droplet and the thickness of the vortex.^{29,43} Figure 3 shows the outline of the measurement. In Figs. 3(a) and 3(b), the velocity in the vicinity of the droplet was calculated using the moving distances of the tracer particles between two consecutive images. Next, the measurement method for vortex thickness at the end of the droplet is shown. As shown in Fig. 3(c), orthogonal coordinates with the center of the

TABLE I. Physical properties of test fluids ($T_s = 300$ K).⁴⁶

| Sample | M (g/mol) | P_{sat} (Pa) | ρ_L (kg/m ³) | ν_L (mm ² /s) | ρ_G (kg/m ³) | ν_G (mm ² /s) | σ (mN/m) |
|---------|-------------|----------------|-------------------------------|------------------------------|-------------------------------|------------------------------|-----------------|
| Decane | 142 | 207 | 23.2 | 1.14 | 6.3 | 0.84 | 23.2 |
| Nonane | 128 | 652 | 22.3 | 0.86 | 5.7 | 0.96 | 22.3 |
| Octane | 114 | 2 060 | 21.0 | 0.71 | 5.1 | 1.13 | 21.0 |
| Heptane | 100 | 6 675 | 19.8 | 0.56 | 4.7 | 1.28 | 19.8 |
| Hexane | 86 | 21 865 | 17.8 | 0.44 | 3.8 | 1.74 | 17.8 |
| Pentane | 72 | 73 168 | 15.3 | 0.86 | 3.2 | 2.18 | 15.3 |

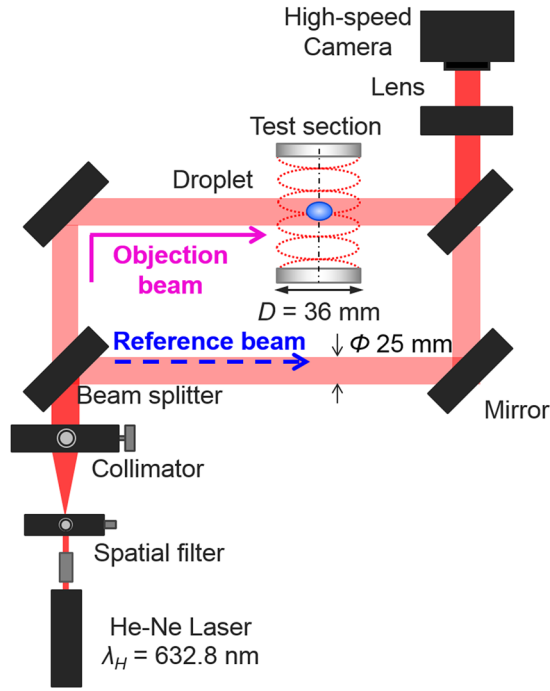


FIG. 2. Schematic of the Mach-Zehnder interferometer.

droplet as the origin are set. Next, by drawing an arbitrary straight line passing through the origin as indicated by the blue lines in the figure, the intersection point of the droplet interface position and the outer edge position of the circulation vortex is obtained. Finally, the distance between the droplet

interface and the circulation vortex outer edge indicated by the pink line is calculated. Perform the above trial five times and let the average of the obtained measurement values be the vortex thickness. Furthermore, the calculated vortex thickness is dimensionless by dividing by the volume equivalent diameter of the droplet.

C. Extraction of phase difference

The method presented by Takeda *et al.*⁴⁷ was adopted to convert a fringe image into the density change in the area. The phase difference between the reference and object beams was correlated with the wavelength as follows:

$$\phi(x, y) = \frac{2\pi\Delta L}{\lambda}. \quad (1)$$

The optical path difference ΔL is expressed as follows:^{45,47,48}

$$\Delta L = \int [n(x, y) - n_0] dl = D \times \Delta n, \quad (2)$$

where Eq. (2) is the difference in the refractive index and the horn diameter $D = 36$ mm. By extracting the phase difference from each image, the refractive index at each point in the image was extracted. Each fringe image was analyzed using the Fourier transform method,⁴⁵ to extract the phase difference between the object and reference beams for each individual pixel, which corresponds to the refractive index in the droplet zone at that point. This process gives a 2D distribution of the refractive index in the droplet zone.⁴⁸ The phase difference contains information on changes in the vapor concentration due to evaporation from the droplet.

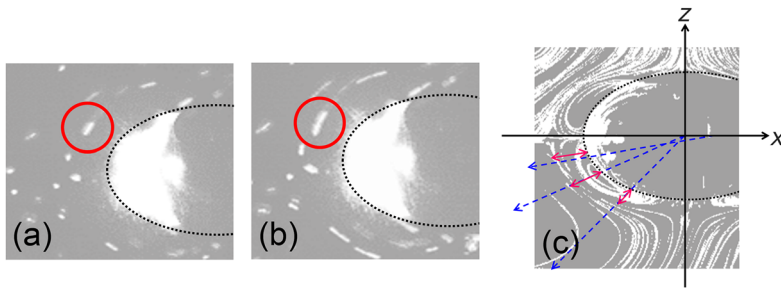


FIG. 3. Measurement method for flow velocity and vortex thickness in the vicinity of the droplet. [(a) and (b)] Flow velocity and (c) vortex thickness.

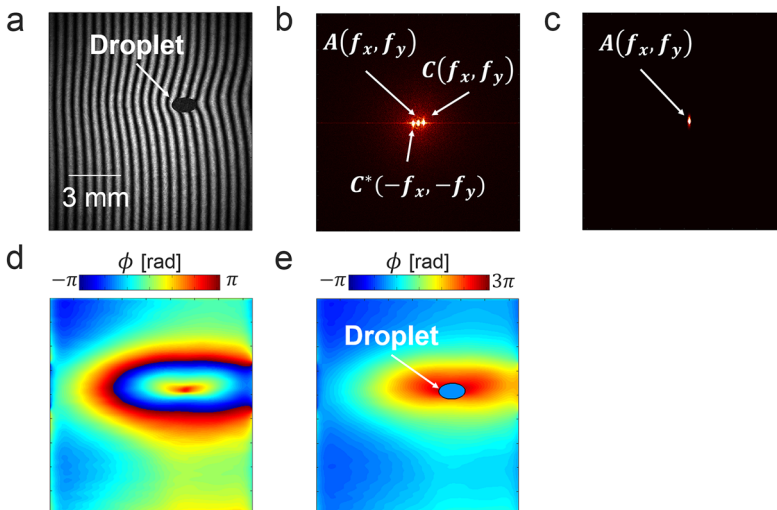


FIG. 4. Procedure for analyzing the phase distribution from fringe images: (a) fringe image, (b) 2D-FFT result, (c) filtered 2D-FFT result, (d) wrapped phase map, and (e) unwrapped phase distribution.

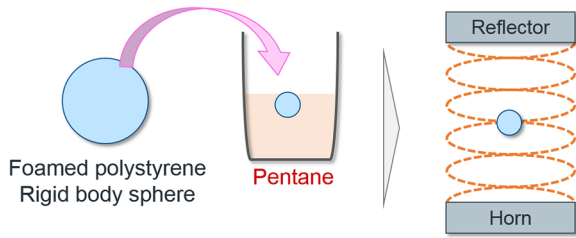


FIG. 5. Experiment using a rigid body sphere.

Figure 4 shows an example of the image processing procedure. The fringe image of a levitated droplet is shown in Fig. 4(a). The shadow at the center of the image is the levitated droplet. To extract the phase distribution from this image, the image was subjected to a two-dimensional fast Fourier transform (2D-FFT), and the result is shown in Fig. 4(b). Next, the 2D-FFT image was filtered to isolate the spectrum that contains the phase information, as shown in Fig. 4(c). A modified Hanning window served as the filter. The spectral distribution in the reference image was obtained by applying the same process. The complex amplitude was obtained using inverse 2D-FFT of the spectral distribution. By using the complex amplitude given above, the interference fringes were extracted, and the result is shown in Fig. 4(d). This leads to a wrapped phase map, which means that the phase range is $-\pi$ to π . Applying an unwrapping algorithm generates a continuous map of the phase distribution. For this, the branch-and-cut method was used.⁴⁹ In brief, the method detects invalid pixels from the integration of the phase difference. Next, unwrapping was performed by avoiding these invalid pixels and their connecting channel when integrating the phase difference. The code for the branch-and-cut method is open-source.⁵⁰ Figure 4(e) shows the resulting unwrapped phase distribution.

D. Experiment using a rigid body sphere

We conducted an experiment using rigid spheres made of polystyrene. The method for visualizing the flow structure and the density change of the surroundings for the rigid body spheres coated with pentane was the same as that for the droplet. In this case, since the volume of test fluids is less than that in the case of the droplet experiment, the phenomenon is quick and it is therefore possible to acquire the transition of the flow structure and density change (Fig. 5).

III. RESULTS

A. Flow structure of droplets

Figure 6 shows the vertical cross sections of the external and internal flow structure around a levitated droplet. The dashed lines show the droplet interface.

Figure 6(A) shows the velocity field inside the droplet obtained using PIV. The recording speed and exposure time were 1000 fps and 0.25 ms, respectively. The spatial resolution was $10.4 \mu\text{m}/\text{pixel}$. The values of the saturated vapor pressure for Figs. 6(A-a)–6(A-d) are lower than those for the others. The internal flows are similar to those of a rigid-body rotation. Figures 6(A-e) and 6(A-f), which correspond to the case of highest saturated vapor pressure, exhibit unsteady 3D complex flow.

Figure 6(B) shows the velocity field outside the droplet obtained using PIV. The recording speed and exposure time were 2000 fps and 0.5 ms, respectively. The spatial resolution was $5.2 \mu\text{m}/\text{pixel}$. In Figs. 6(B-a) and 6(B-b), at a low saturated vapor pressure, the flow velocity around the droplet seems to be large. Although the flow velocity is decreased in Figs. 6(B-c) and 6(B-d), it increases again in Figs. 6(B-e) and 6(B-f).

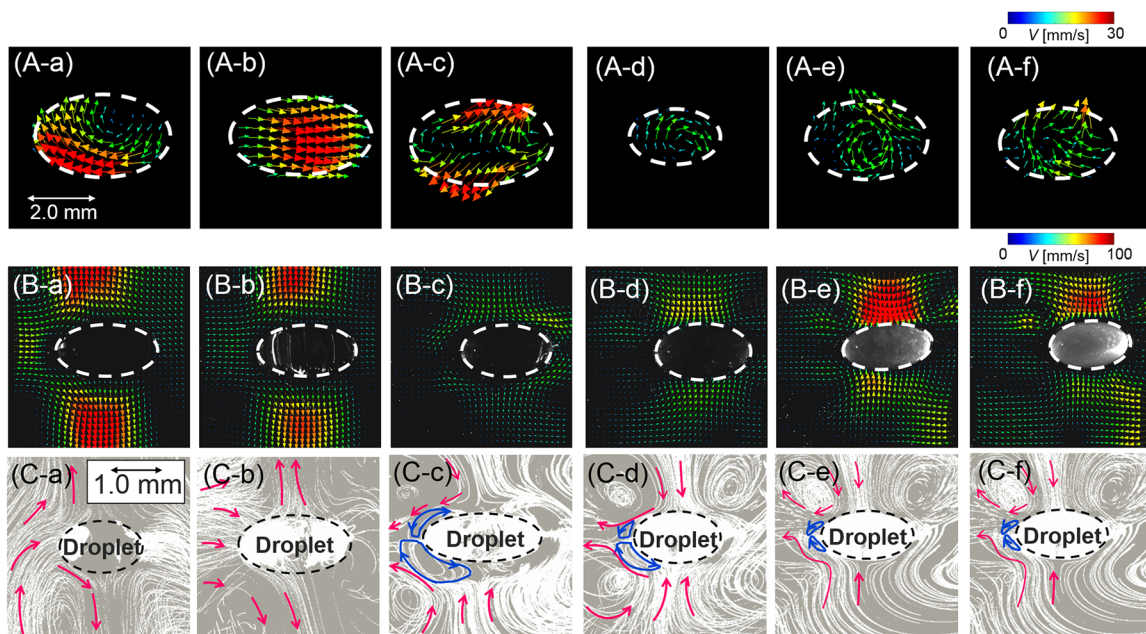


FIG. 6. Flow structure around acoustically levitated droplets: (A) velocity vector fields inside droplets, (B) velocity vector fields outside droplets, and (C) flow direction of the external flow around the levitated droplets. Pink lines show the external flow structure. Blue lines show the circular vortex. (a) Decane, (b) nonane, (c) octane, (d) heptane, (e) hexane, and (f) pentane.

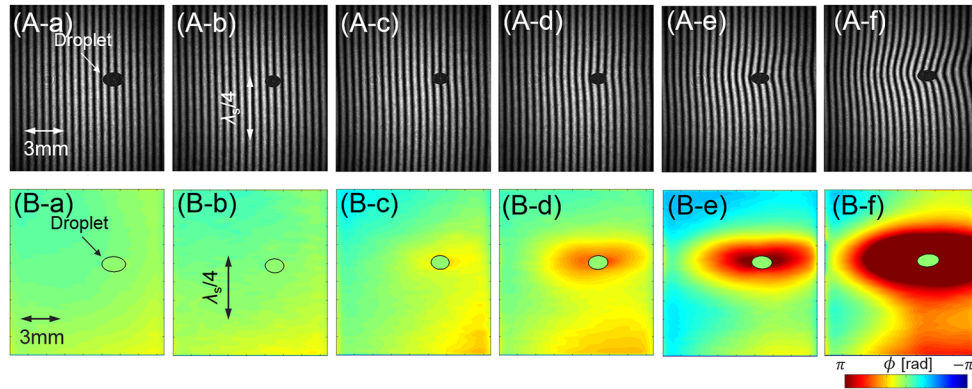


FIG. 7. Results of contactless density field measurement by using a Mach–Zehnder interferometer: (λ_s is the wavelength of a standing wave). (A) The change of interference fringes around each droplet and (B) phase difference distribution around each droplet. (a) Decane, (b) nonane, (c) octane, (d) heptane, (e) hexane, and (f) pentane.

Figure 6(C) shows the direction of the external flow around the levitated droplet. The recording speed and exposure time were 4000 fps and 0.25 ms, respectively. The spatial resolution was $10.4 \mu\text{m}/\text{pixel}$. The white curves show the paths of the particles from multiple exposures taken 0.1 s apart. The arrows show the direction of the external flow. Note that the arrow length does not correspond to the magnitude of the flow velocity. The patterns of the external flow in Figs. 6(C-a) and 6(C-b) differ drastically from those in Figs. 6(C-c)–6(C-f). More precisely, the direction of the external flow in Figs. 6(C-a) and 6(C-b) is from the surface of each droplet. Conversely, in Figs. 6(C-c)–6(C-f), the direction of the external flows is from the top or bottom of the image toward each droplet. In addition, a circular vortex of decreasing size appears near the droplet interfaces in Figs. 6(C-c)–6(C-f).

B. Phase change behavior

Figure 7(A) shows the images of the original fringe pattern around the levitated droplets. The recording speed was 4000 fps and the shutter speed was $7.8 \mu\text{s}$, which is sufficiently faster than the sound frequency of $\sim 52.6 \mu\text{s}$. The spatial resolution was $14.5 \mu\text{m}/\text{pixel}$. The sound intensity was 160 dB. The fringe patterns in Figs. 7(A-a) and 7(A-b) (low saturated vapor pressure) are uniform; however, they gradually change

as the saturated vapor pressure increases from Figs. 7(A-c) to 7(A-f). Figure 7(B) shows the time-averaged phase distribution around the levitated droplets, as obtained from the original images in Fig. 7(A). The reference point for phase extraction was at a node of the sound pressure amplitude and was sufficiently far from the levitated droplet. To compare the results, the data were averaged over a 12.5-ms period. The results show that the phase increases with increasing saturated vapor pressure.

IV. DISCUSSION

As shown in Fig. 6, the external flow structure of the droplet changes as the saturated vapor pressure increases. Next, we focus on the flow structure in the vicinity of the droplet interface. Figures 8(a) and 8(b) show the results of the measured velocity in the vicinity of the droplet interface and the thickness of the circular vortex as a function of the saturated vapor pressure. From these figures, we noted that the velocity in the vicinity of the droplet and the thickness of the vortex decrease with increasing saturated vapor pressure.

In Sec. III B, we saw that the phase difference around droplets increases with increasing saturated vapor pressure. Tables II and III show the density change accompanying the

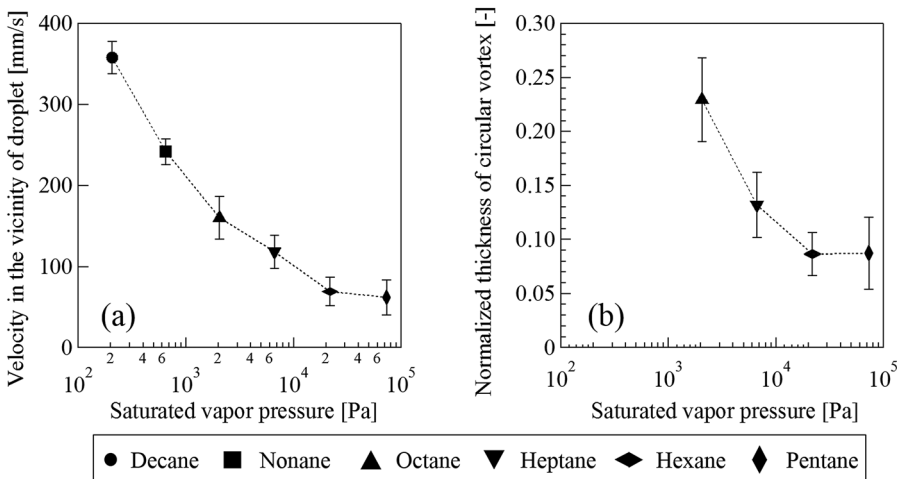


FIG. 8. Quantitative evaluation of flow structure: (a) Flow velocity in the vicinity of the droplet surface and (b) thickness of the circular vortex.

TABLE II. Change in air density with temperature.

| Temperature (°C) | Density (kg/m ³) | Relative vapor |
|------------------|------------------------------|----------------|
| 20 | 1.19 | 1 |
| 0 | 1.293 | 1.09 |
| -10 | 1.342 | 1.13 |

TABLE III. Change in air density with temperature.

| Sample | Relative vapor density |
|---------|------------------------|
| Air | 1 |
| Octane | 4.25 |
| Pentane | 2.66 |

temperature change and the change in the gas phase component. When comparing Tables II and III, the influence of a change in temperature on the density change of a gas is smaller than that of a change in the gas phase component. Thus, we can consider that the phase change shown in Fig. 7(B) mainly describes the density change due to evaporation of the droplet. Figure 9 shows the averaged phase value near the droplet

interface as a function of the saturated vapor pressure. We can clearly observe that the phase differences near the droplet interface increase with increasing saturated vapor pressure. From this, we conceive that the density change around the droplet is larger for droplets with a higher saturated vapor pressure. As the density around the droplet changes, the kinematic viscosity also changes. The kinematic viscosity of air is $\nu_{Air} = 15 \text{ mm}^2/\text{s}$ and that of the test fluid vapor is lower than that. From this, we conceive that as the saturated vapor pressure increases, the amount of evaporation of the droplet increases and the kinematic viscosity around the droplet decreases. Therefore, we consider that as the saturated vapor pressure increases, both the flow velocity in the vicinity of the droplet and the vortex thickness decrease.

We also conducted experiments using polystyrene rigid body spheres coated with pentane. Figure 10 shows the transition of the flow structure and the phase difference distribution around the rigid body sphere coated with pentane. As shown in Fig. 10(a), the flow structure of the rigid body sphere coated with pentane has the same flow structure as the pentane droplet in Fig. 6(C-f). However, as shown in Fig. 10(b), the circular vortex expanded with passage of time. Finally, as shown in Fig. 10(c), the flow structure resembled that of

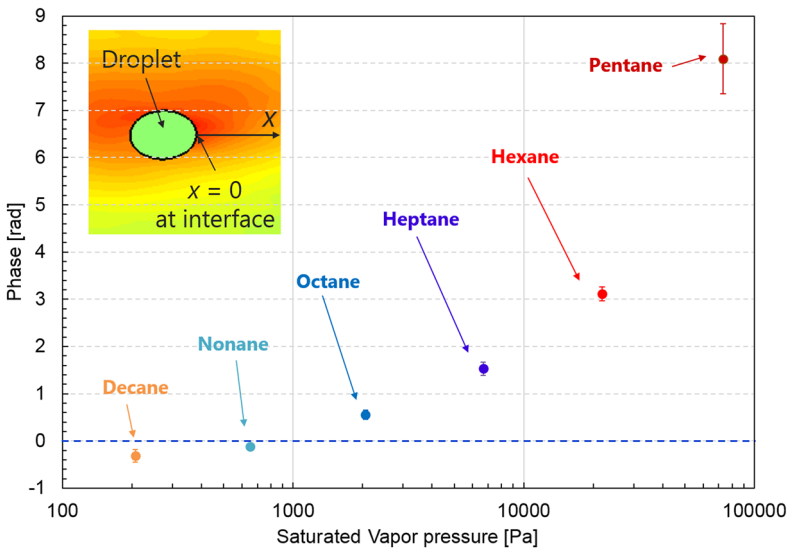


FIG. 9. Phase difference at the right end of each droplet.

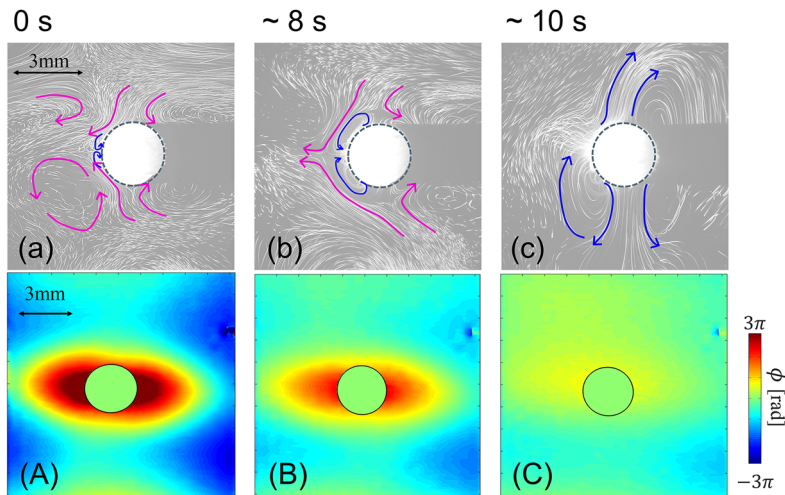


FIG. 10. Change in the flow structure and phase-difference distribution around a rigid body sphere coated with pentane: [(a)–(c)] external flow structure and [(A)–(C)] phase-difference distribution.

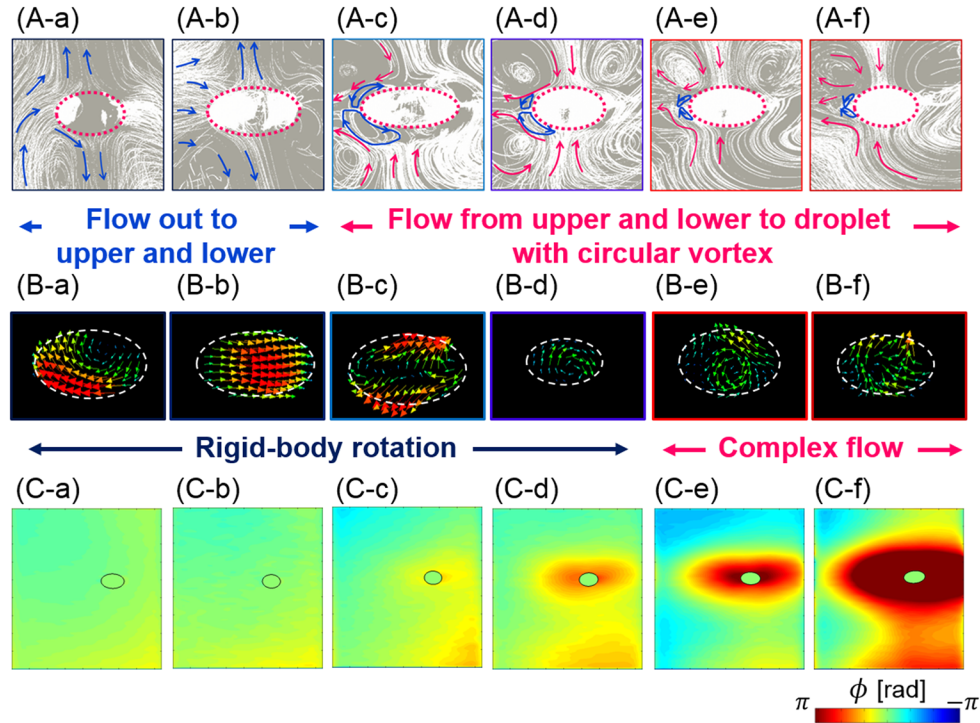


FIG. 11. Flow structure and phase-difference distribution around the droplet: (A) External flow structure. Red lines show the external flow structure. Blue lines show the circular vortex, (B) Internal flow structure. (C) Phase-difference distribution. (a) Decane, (b) nonane, (c) octane, (d) heptane, (e) hexane, and (f) pentane.

the decane droplet in Fig. 6(C-a). From this, we can see that the flow structure around the sample changes by expanding the circulation vortex. In addition, as shown in Figs. 10(A)–10(C), the phase difference around the rigid body sphere decreases over time. Although this is the result of the solid sphere, it suggests that the density change around the sample had an influence on the flow structure.

Figure 11 summarizes our experimental results for the external flow, internal flow, and time-averaged phase distribution. At a low saturated vapor pressure [Figs. 11(A-a) and 11(A-b)], the external flow travels from the droplet toward the top or bottom of the image. However, at a high saturated vapor pressure, the external flow travels from the top and bottom of the images toward the droplet surface, with a circular vortex forming near the droplet surface. Under conditions of a low saturated vapor pressure [Figs. 11(B-a)–11(B-d)], the internal flow is similar to that in the case of rigid body rotation. Finally, under conditions of the high saturated vapor pressure [Figs. 11(B-e) and 11(B-f)], the internal flow is an unsteady 3D complex flow. In addition, as the saturated vapor pressure increases, the phase difference around the droplet increases [Figs. 11(C-a)–11(C-f)].

We also measured the velocity near the interface of droplets and the thickness of the circulation vortex from these visualization results. The velocity in the vicinity of the droplet and the thickness of the circulation vortex decreased with increasing saturated vapor pressure (Fig. 8). This change is attributed to a change in the kinematic viscosity around the droplet due to evaporation of the droplet. From these results, we conclude that it is possible that the flow structure of the acoustically levitated droplet changes due to the change in the

kinematic viscosity around the droplet through evaporation of the droplet.

Furthermore, by using a rigid body ball coated with pentane, we elucidated that the flow structure changes as the circulation vortex expands.

V. CONCLUSION

Our observations show that the internal and external flow fields change as the saturated vapor pressure changes. For a low saturated vapor pressure (decane and nonane), the external flow originates from the surface of each droplet. However, for a relatively higher saturated vapor pressure (octane, heptane, hexane, and pentane), the external flow originates from the top and bottom of the droplet along the droplet surface and accompanies the formation of a circular vortex. In addition, both the flow velocity near the interface and the circulation vortex thickness decrease with increasing saturated vapor pressure. For a low saturated vapor pressure (decane, nonane, octane, and heptane), the internal flow is similar that in the case of rigid body rotation. For a high saturated vapor pressure (hexane and pentane), the internal flow is an unsteady 3D complex flow.

In order to clarify the effect of saturated vapor pressure on the droplet, we visualized the phase-difference distribution around the surface of an acoustically levitated volatile droplet using a Mach–Zehnder interferometer. The results show that the phase difference increases with increasing saturated vapor pressure, indicating that the vapor concentration around a levitated droplet increases with increasing saturated vapor pressure.

These experimental results provided us with the crucial ingredient to determine the vapor concentration around the acoustically levitated droplet. In the future, these findings may contribute to further the development of contactless manipulation techniques of droplets and their existing theoretical predictions.

VI. STATISTICAL ANALYSIS

The error of the droplet diameter could be a maximum of 5% because the levitated droplets were observed with a spatial resolution of $10 \pm 5 \mu\text{m}/\text{pix}$. The velocity in the vicinity of the droplet and the thickness of the vortex in Fig. 8 were measured five times for each sample; the average of the data obtained from a total of three samples was used as a representative value. Error bars represent standard deviations and are obtained using the following equation:

$$s = \sqrt{\frac{1}{n} \sum_{i=1}^n (x_i - \bar{x})^2}. \quad (3)$$

The average phase difference at the end of the droplet is the average of the phase difference taken from 20 images and is taken as the representative value. Error bars are standard deviations, as shown in Eq. (3).

ACKNOWLEDGMENTS

This work was supported by JSPS KAKENHI Grant Nos. 16360097, 18360083, 23360081, and 15H03925. The authors thank Dr. Satoshi Matsumoto, Professor Katsuhiko Nishinari, Professor Tadashi Watanabe, Professor Hiroyuki Kitahata, and Professor Akiko Kaneko for their insightful comments and suggestions.

- ¹E. H. Brandt, "Acoustic physics: Suspended by sound," *Nature* **413**, 474 (2001).
- ²F. Priego-Capote and L. de Castro, "Ultrasound-assisted levitation: Lab-on-a-drop," *Trends Anal. Chem.* **25**, 856 (2006).
- ³D. Foresti and D. Poulikakos, "Acoustophoretic contactless elevation, orbital transport and spinning of matter in air," *Phys. Rev. Lett.* **112**, 024301 (2014).
- ⁴D. Foresti, M. Nabavi, M. Klingauf, A. Ferrari, and D. Poulikakos, "Acoustophoretic contactless transport and handling of matter in air," *Proc. Natl. Acad. Sci. U. S. A.* **110**, 12549 (2013).
- ⁵S. Tsujino and T. Takashi, "Ultrasonic acoustic levitation for fast frame rate X-ray protein crystallography at room temperature," *Sci. Rep.* **6**, 25558 (2016).
- ⁶T. Vasileiou, D. Foresti, A. Bayram, D. Poulikakos, and A. Ferrari, "Toward contactless biology: Acoustophoretic DNA transfection," *Sci. Rep.* **6**, 20023 (2016).
- ⁷A. Marzo, S. Seah, B. Drinkwater, D. Sahoo, B. Long, and S. Subramaniam, "Holographic acoustic elements for manipulation of levitated objects," *Nat. Commun.* **6**, 8661 (2015).
- ⁸V. Vandaale, P. Lambert, and A. Delchambre, "Non-contact handling in microassembly: Acoustical levitation," *Precis. Eng.* **29**, 491 (2005).
- ⁹E. H. Trinh and J. L. Robey, "Experimental study of streaming flows associated with ultrasonic levitators," *Phys. Fluids* **6**, 3567 (1994).
- ¹⁰A. Y. Rednikov and N. Riley, "A simulation of streaming flows associated with acoustic levitators," *Phys. Fluids* **14**, 1502 (2002).
- ¹¹H. Zhao, S. S. Sadhal, and E. H. Trinh, "Singular perturbation analysis of an acoustically levitated sphere: Flow about the velocity node," *J. Acoust. Soc. Am.* **106**, 589 (1999).
- ¹²H. Zhao, S. S. Sadhal, and E. H. Trinh, "Internal circulation in a drop in an acoustic field," *J. Acoust. Soc. Am.* **106**, 3289 (1999).
- ¹³A. L. Yarin, M. Pfaffenlehner, and C. Tropea, "On the acoustic levitation of droplets," *J. Fluid Mech.* **356**, 65 (1998).
- ¹⁴S. D. Danilov and M. A. Mironov, "Breakup of a droplet in a high-intensity sound field," *J. Acoust. Soc. Am.* **92**, 2747 (1992).
- ¹⁵Z. L. Yan, W. J. Xie, and B. Wei, "Vortex flow in acoustically levitated drops," *Phys. Lett. A* **375**, 3306 (2011).
- ¹⁶A. Saha, S. Basu, and R. Kumar, "Velocity and rotation measurements in acoustically levitated droplets," *Phys. Lett. A* **376**, 3185 (2012).
- ¹⁷L. Puskar, R. Tuckermann, T. Frosch, J. Popp, V. Ly, D. McNaughton, and B. R. Wood, "Raman acoustic levitation spectroscopy of red blood cells and *Plasmodium falciparum* trophozoites," *Lab Chip* **7**, 1125 (2007).
- ¹⁸W. J. Xie, C. D. Cao, Y. J. Lü, Z. Y. Hong, and B. Wei, "Acoustic method for levitation of small living animals," *Appl. Phys. Lett.* **89**, 214102 (2006).
- ¹⁹M. Sundvik, H. J. Nieminen, A. Salmi, P. Panula, and E. Hægström, "Effects of acoustic levitation on the development of zebrafish, *Danio rerio*, embryos," *Sci. Rep.* **5**, 13596 (2015).
- ²⁰E. T. Chainani, W. H. Choi, K. T. Ngo, and A. Scheeline, "Mixing in colliding, ultrasonically levitated drops," *Anal. Chem.* **86**, 2229 (2014).
- ²¹C. Bouyer, P. Chen, S. Güven, T. T. Demirtaş, T. J. F. Nieland, F. Padilla, and U. Demirci, "A bio-acoustic levitational (BAL) assembly method for engineering of multilayered, 3D brain-like constructs, using human embryonic stem cell derived neuro-progenitors," *Adv. Mater.* **28**, 161 (2016).
- ²²D. Foresti, M. Nabavi, and D. Poulikakos, "On the acoustic levitation stability behaviour of spherical and ellipsoidal particles," *J. Fluid Mech.* **709**, 581 (2012).
- ²³Y. Abe, Y. Yamamoto, D. Hyuga, S. Awazu, and K. Aoki, "Study on interfacial stability and internal flow of a droplet levitated by ultrasonic wave," *Ann. N. Y. Acad. Sci.* **1161**, 211 (2009).
- ²⁴A. Y. Rednikov and S. S. Sadhal, "Steady streaming from an oblate spheroid due to vibrations along its axis," *J. Fluid Mech.* **499**, 345 (2004).
- ²⁵A. Y. Rednikov and S. S. Sadhal, "Acoustic/steady streaming from a motionless boundary and related phenomena: Generalized treatment of the inner streaming and examples," *J. Fluid Mech.* **667**, 426 (2011).
- ²⁶A. Y. Rednikov, H. Zhao, S. S. Sadhal, and E. H. Trinh, "Steady streaming around a spherical drop displaced from the velocity antinode in an acoustic levitation field," *Q. J. Mech. Appl. Math.* **59**, 377 (2006).
- ²⁷Y. Yamamoto, Y. Abe, A. Fujiwara, K. Hasegawa, and K. Aoki, "Internal flow of acoustically levitated droplet," *Microgravity Sci. Technol.* **20**, 277 (2008).
- ²⁸K. Hasegawa, A. Kaneko, K. Aoki, and Y. Abe, "PIV measurement of internal and external flow of an acoustically levitated droplet," *Int. J. Trans. Phenom.* **12**, 151 (2011).
- ²⁹K. Shitanishi, K. Hasegawa, A. Kaneko, and Y. Abe, "Study on heat transfer and flow characteristic under phase-change process of an acoustically levitated droplet," *Microgravity Sci. Technol.* **26**, 305 (2014).
- ³⁰A. L. Yarin, G. Brenn, O. Kastner, D. Rensink, and C. Tropea, "Evaporation of acoustically levitated droplets," *J. Fluid Mech.* **399**, 151 (1999).
- ³¹A. L. Yarin, G. Brenn, O. Kastner, and D. Rensink, "Evaporation of acoustically levitated droplets of binary liquid mixtures," *Int. J. Heat Fluid Flow* **23**, 471 (2002).
- ³²E. Welter and B. Neidhart, "Acoustically levitated droplets—A new tool for micro and trace analysis," *Fresenius' J. Anal. Chem.* **357**, 345 (1997).
- ³³R. Tuckermann, S. Bauerecker, and B. Neidhart, "Evaporation rates of alkanes and alkanols from acoustically levitated drops," *Anal. Bioanal. Chem.* **372**, 122 (2002).
- ³⁴R. Tuckermann, S. Bauerecker, and H. K. Cammenga, "IR-thermography of evaporating acoustically levitated drops," *Int. J. Thermophys.* **26**, 1583 (2005).
- ³⁵J. J. Hegseth, N. Rashidnia, and A. Chai, "Natural convection in droplet evaporation," *Phys. Rev. E* **54**, 1640 (1996).
- ³⁶C. K. Law, T. Y. Xiong, and C. H. Wang, "Alcohol droplet vaporization in humid air," *Int. J. Heat Mass Transfer* **30**, 1435 (1987).
- ³⁷W. E. Ranz and W. R. Marshall, "Evaporation from drops: Part 1," *Chem. Eng. Prog.* **48**, 141 (1952).
- ³⁸W. E. Ranz and W. R. Marshall, "Evaporation from drops: Part 2," *Chem. Eng. Prog.* **48**, 173 (1952).
- ³⁹S. Somasundaram, T. N. C. Anand, and S. Bakshi, "Evaporation-induced flow around a pendant droplet and its influence on evaporation," *Phys. Fluids* **27**, 112105 (2015).
- ⁴⁰B. He and F. Duan, "Evaporation and convective flow pattern of a heated pendant silicone oil droplet," *Int. J. Heat Mass Transfer* **85**, 910 (2015).

- ⁴¹S. Dash, A. Chandramohan, J. A. Weibel, and S. V. Garimella, "Buoyancy-induced on-the-spot mixing in droplets evaporating on nonwetting surfaces," *Phys. Rev. E* **90**, 062407 (2014).
- ⁴²H. Ishii, K. Hasegawa, A. Kaneko, and Y. Abe, "Internal and external flow structure and mass transport phenomena of an acoustically levitated droplet," *Trans. Jpn. Soc. Mech. Eng. Ser. B* **78**, 1696 (2012).
- ⁴³A. Goda, K. Hasegawa, A. Kaneko, T. Kanagawa, and Y. Abe, "External flow structure and interfacial transport phenomena of an acoustically levitated droplet," *Jpn. J. Multiphase Flow* **28**, 539 (2015).
- ⁴⁴K. Hasegawa, A. Goda, and Y. Abe, "Microlayered flow structure around an acoustically levitated droplet under a phase-change process," *npj Microgravity* **2**, 16004 (2016).
- ⁴⁵T. Kreis, "Digital holographic interference-phase measurement using the Fourier-transform method," *J. Opt. Soc. Am. A* **3**, 847 (1986).
- ⁴⁶E. W. Lemmon *et al.*, NIST Standard Reference Database 23, version 9.0, 2013.
- ⁴⁷M. Takeda, H. Ina, and S. Kobayashi, "Fourier-transform method of fringe-pattern analysis for computer-based topography and interferometry," *J. Opt. Soc. Am.* **72**, 156 (1982).
- ⁴⁸S. Dehaeck, A. Rednikov, and P. Colinet, "Vapor-based interferometric measurement of local evaporation rate and interfacial temperature of evaporating droplets," *Langmuir* **30**, 2002 (2014).
- ⁴⁹R. M. Goldstein, H. A. Zebker, and C. L. Werner, "Satellite radar interferometry: Two-dimensional phase unwrapping," *Radio Sci.* **23**, 713, <https://doi.org/10.1029/rs023i004p00713> (1988).
- ⁵⁰The MathWorks, Inc., MATLAB CENTRAL, File Exchange, <http://www.mathworks.com/matlabcentral/fileexchange/22504-2d-phase-unwrapping-algorithms> (last accessed December 21, 2016).